Journal of Oceanology and Limnology
Vol. 44, No. 3, pp. 950-962, 2026
https://doi.org/10.1007/s00343-025-5140-y

Research Paper

Rogue waves in the northern part of the South China Sea: chaotic dynamics and multiparameter synergy determination*

Tao FENG[1, 2, 3, 4, 5], Tianyu ZHANG[1, 2, 3, 4, 5, **], Danchen YAN[6], Hailong WANG[1, 2, 3, 4, 5], Jian YANG[1, 2, 3, 4, 5], Xun LIN[1, 2, 3, 4, 5], Junping ZHANG[1, 2, 3, 4, 5]

[1] *College of Ocean and Meteorology, Guangdong Ocean University, Zhanjiang 524088, China*

[2] *Laboratory for Coastal Ocean Variation and Disaster Prediction, College of Ocean and Meteorology, Guangdong Ocean University, Zhanjiang 524088, China*

[3] *Key Laboratory of Climate, Resources and Environment in Continental Shelf Sea and Deep Sea of Department of Education of Guangdong Province, Guangdong Ocean University, Zhanjiang 524088, China*

[4] *Key Laboratory of Space Ocean Remote Sensing and Application, Ministry of Natural Resources, Beijing 100081, China*

[5] *Tropical Ocean Environment in Western Coastal Waters Observation and Research Station of Guangdong Province, Guangdong Ocean University, Zhanjiang 524088, China*

[6] *National Marine Environmental Forecasting Center, Beijing 100081, China*

Received May 7, 2025; accepted in principle Jul. 9, 2025; accepted for publication Aug. 25, 2025

Abstract Based on wave data recorded in 2020 from 10 buoy stations in the northern part of the South China Sea, the synergistic effects of wave parameters such as wave steepness, spectral width, kurtosis, skewness and Benjamin-Feir index (BFI) on a rogue wave group in the northern waters of the South China Sea were investigated. The frequency and energy distributions of three types of rogue waves were recognized based on wavelet transform. Chaotic dynamics was introduced to study the chaotic phenomena in the wave series where rogue wave were located. Results show that wave steepening enhanced the nonlinear effect of waves, and a narrow spectrum could suppress the dispersion effect, which increased the BFI, triggered the modulation instability of waves, and promoted the generation of distorted waves. When kurtosis>3, the BFI increases as the degree of kurtosis deviation from the Gaussian distribution increases. In particular, when kurtosis>3 and $H/H_s>2.2$, the increase in kurtosis contributes significantly to the increase in the anomalous intensity of the rogue wave. Rogue waves induced by modulation instability and those induced by the superposition of wave clusters can be explained by phase and dispersion modulation as well as by energy distribution, whereas the generation mechanism of rogue waves that have not grown sufficiently is difficult to resolve from the time-domain waveform characteristics and the frequency-domain wavelet energy density. Qualitative analysis by the Poincaré cross section and quantitative analysis by the Lyapunov exponent verified that the nonlinear wave system, in which a rogue wave is located in the wave train, has weakly chaotic dynamic behavior.

Keyword: northern South China Sea; rogue wave; wave parameter threshold; energy distribution; chaotic dynamic

---

* Supported by the National Natural Science Foundation of China (Nos. 42476219, 42401111, 41976200), the National Foreign Experts Program (No. S20240134), the National Key Research and Development Program of China (Nos. 2021YFC3101801, 2023YFC3008200), the Innovative Team Plan of the Department of Education of Guangdong Province (No. 2023KCXTD015), the Tropical Ocean Environment in Western Coastal Waters Observation and Research Station of Guangdong Province (No. 2024B1212040008), the Project supported by Southern Marine Science and Engineering Guangdong Laboratory (Zhuhai) (Nos. SML2022SP301, SML2024SP023), the Innovative Programs for Ordinary Higher Education Institutions in Guangdong Province (No. 2024KTSCX200), the Shandong Innovation and Development Research Institute Think Tank Project, and the Guangdong Ocean University Start-up Scientific Research Program (Nos. 060302032106, 060302032104)

** Corresponding author: zhaangty@sina.com

1 INTRODUCTION

Fluctuation in the ocean often forms clusters, and waves occasionally develop asymmetrical crests that are much greater than regular waves. Waves whose height is greater than or equal to two times of the effective wave height are defined as rogue waves. This particular hydrodynamic phenomenon is very destructive and seriously hazardous to offshore constructions, marine vessels, and so on. Rogue waves, as an extreme marine phenomenon, are notorious for causing many disasters in the North Atlantic Ocean, the southern Indian Ocean, and other seas (Pei, 2008). In recent years, several anomalous wave conditions have also been observed in deep-water areas of the South China Sea (Chen et al., 2019), and the occurrence of these wave-induced disasters calls for the urgent need to carry out research on the mechanism of aberrant wave generation in the field of ocean engineering safety. For examples, the Draupner event with a peak wave height of 25.6 m in the Norwegian Sea in 1995 (Cavaleri et al., 2016), and the extreme wave height of 34 m recorded during Typhoon Haiyan in 2013 (Yin and Liang, 2014), posed serious challenges to traditional wave theory.

Research results on rogue waves are abundant, but the resolution of the physical mechanisms behind them still lacks clarity. Common mechanisms for generating rogue waves include temporal focusing due to dispersion, spatial focusing, the effect of modulation instability, and the interaction among waves (Pelinovsky and Kharif, 2016; Li et al., 2020; Ma et al., 2020; He et al., 2021), essentially unfolding; these mechanisms cover two main scopes: traditional linear wave theory that based on the assumption of a smooth stochastic process and nonlinear generation theory based on kinetic methods. Although these theories can intuitively illustrate the generation of rogue waves and be described in kinematic way, they do not involve nonlinear dynamical processes such as wave breaking and wave interactions (Liu et al., 2013), and cannot explain the strong transient characteristics of rogue waves. Therefore, we analyzed the current generation mechanism of rogue waves in indicates the strong nonlinearity of rogue waves, and the suddenness nature reflects the instability of the wave motion. From a kinetic point of view, wave motion is affected by external forces such as gravity, wind forcing, and bottom friction. It is difficult for an external drive to input a large amount of energy to the wave in a short period, whereas the enormous and sudden nature of rogue waves energy in the ocean indicates that the external drive is a pre-triggering factor for the generation of rogue waves (Ke et al., 2021). Touboul et al. (2006) first considered the effect of wind field forcing on the generation of rogue waves, and their results show that the effect of wind field forcing on the generation of rogue waves is weak, and more effects are build up before the generation of rogue waves. Davis (1966) simulated focused waves based on the dispersion-focusing mechanism by adjusting the phase of each component of a wave to focus on a specific moment. Zhao et al. (2009) investigated the rogue wave evolution in three dimensions in numerical and physical simulation experiments. Based on the theory of the Benjamin-Feir instability, Dyachenko and Zakharov (2005) scrutinized the instability of Stokes waves under sideband perturbation conditions and analyzed the process of rogue wave evolution. Onorato et al. (2004) defined the Benjamin-Feir index (BFI) and simulated a random wave train with different BFIs in a wave flume experiment, and concluded that the BFI is an important parameter indicating the generation of rogue waves. Li et al. (2020) concluded by conducting numerical experiments that when the wave steepness parameter exceeds 0.1, the modulation instability caused by higher-order nonlinear effects can lead to a sudden increase of the wave packet energy of more than 40% within several times the wave period. Zakharov (1968) investigated the nonlinear modulation of deep-water wave trains using wave Hamiltonian theory combined with the third-order nonlinear Schrödinger equation. Kriebel et al. (2000) proposed a two-wave train superposition model, in which the fundamental and transient wave trains are superimposed to produce rogue waves, explored the physical mechanisms related to wave instability in detail, and laid the foundation for the in-depth study of rogue waves. However, owing to the scarcity of measured wave data, most current generation mechanisms for rogue waves are based on numerical and physical modeling experiments. In real marine environment, the formation of rogue waves may involve a combination of multiple mechanisms, and ocean waves have significant randomness, so there is a certain difference between the theoretical and real sea conditions. Field observations can provide empirical support for research on the statistical characteristics and generation mechanisms of rogue waves. Based on

10-year observational data from the Norwegian Sea, Fu et al. (2024) analyzed more than 1 million unidirectional wave clusters measured in the deep waters of the Norwegian Sea, and for the first time, they classified the wave clusters into two categories: normal wave clusters and rogue wave clusters based on whether they contained rogue waves. They found that both the distributions of the non-dimensional group energy and group duration followed the generalized extreme value functions. Moreover, the statistics of wave groups are significantly influenced by the spectral width, and the effect of wave steepness was negligible. Knobler et al. (2022) statistically analyzed deep-water buoy observational data from two severe storms in the Eastern Mediterranean Sea in 2017 and 2018, and found that the maximum waves in this sea area had similar characteristics to typical rogue waves such as Draupner, Andrea, and EI Faro, in which the second order bound nonlinearities enhanced the linear dispersive focusing of rogue waves. The above observational studies revealed regional differences in energy distribution, morphological characteristics, and risk probability of rogue waves in different sea areas, and provided important observational benchmark data for the study of rogue waves.

The northern part of the South China Sea, as the core power region of the western Pacific marginal sea, is not only an important corridor for maritime energy transportation, but also a sensitive area for the interaction between the global monsoon system and the Kuroshio branch (Zhang, 2019). The complex topographic features of this sea area coupled with multiscale dynamic processes make it a high incidence area for extreme wave events. In this study, on the basis of buoy data from the northern part of the South China Sea, the wave parameters of the rogue waves in this sea area were analyzed in combination with the BFI, and the nonlinear dynamic process and energy distribution of the three types of rogue waves were investigated via wavelet transform, and chaotic dynamics were introduced to study the generation mechanism of the rogue waves.

2 MATERIAL AND METHOD

2.1 Data and sea state

In this study, real-time raw data recorded at 10 buoy stations in the northern part of the South China Sea were used, with a sampling frequency of 1 Hz and a post-sampling data recorded in 30-min interval at the buoy stations, and the main body of the observational data was collected from January 2020 to December 2020. Quality control of data is essential to minimize false information caused by unavoidable measurement errors. A total of 111 655 sets of wave data were extracted from the buoy observation real-time data files, and after data quality control (Yang et al., 2017) to remove outliers caused by sensor anomalies, 109 724 sets of wave data were obtained, of which 627 sets contained rogue waves. Table 1 shows the wave observations from the buoy stations obtained after screening and eliminating the original suspect data, where the number of data is 30-min long time series.

The South China Sea is famous for its complex topography and sea state, and the research area of this study is the northern part of the South China Sea (Fig.1). The width of its continental shelf is significantly narrowed from west to east, and the topographic effect is significant. At the same time, the influence of the monsoon leads to strong wind and wave activity in this area, and this kind of topographic gradient and complex hydrodynamic characteristics can provide a natural experimental field for the study of abnormal waves.

2.2 Data processing and classification

The determination of rogue waves is based on a “wave height greater than or equal to 2 times the effective wave height”, i.e.,

$$H/H_s \geq 2, \quad (1)$$

where H is the wave height and H_s is the effective wave height in meter.

Figure 2 shows the boxplot statistics of the ratio of the maximum wave height H_{max} to the effective

Table 1 Observatory data situation

Buoy station	Number of rogue wave	Number of data
S1	68	8 855
S2	39	9 930
S3	142	17 150
S4	88	10 906
S5	50	10 684
S6	53	9 814
S7	72	12 240
S8	53	10 709
S9	14	9 640
S10	48	9 796

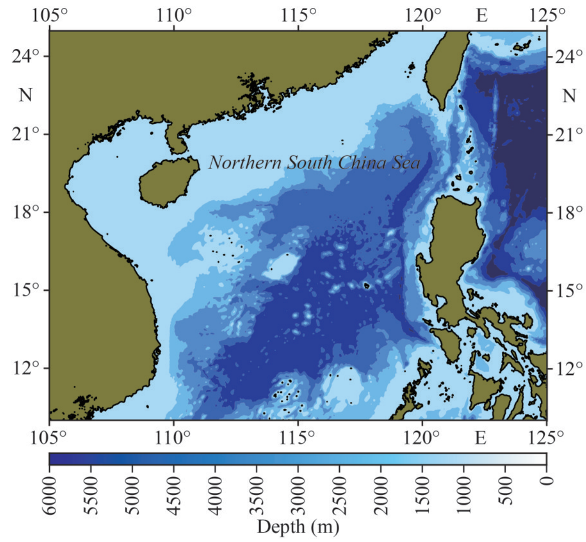

Fig.1 The study area

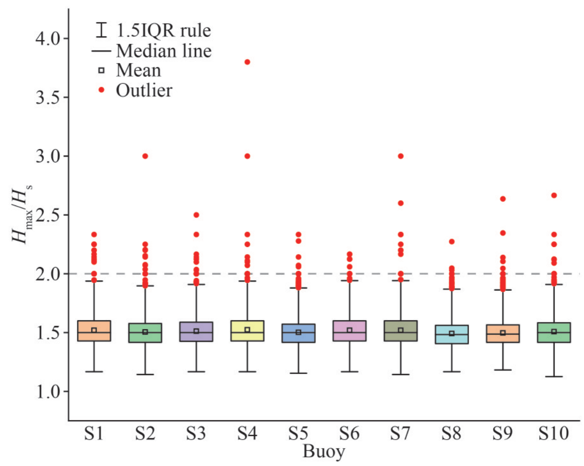

Fig.2 The statistical results of wave height ratio in each buoy station

wave height for each wave train recorded at 10 buoy stations in the northern part of the South China Sea, where the red outliers with ratios greater than or equal to 2 are the wave trains where the rogue waves are located. Overall, the median ratios of the sites ranged from 1.4 to 1.6, but the anomaly ratios in different topographic subdivisions significantly differed. This phenomenon may be a nonlinear modulation of the wave extreme value structure by topographic gradients and local hydrodynamic processes. Anomalously high values with ratios greater than or equal to 2, i.e., the presence of anomalous wave heights, were detected at all stations. The spatial heterogeneity of the ratios at individual buoy stations suggests that a topographic parameterization scheme needs to be introduced into the traditional statistical model of wave polarity.

To better present the rogue wave characteristics, three typical examples of rogue waves are further analyzed as illustrated in Fig.3, namely, abnormally elevated peaks (P1), nearly symmetrical peaks and valleys (P2), and abnormally deepened valleys (P3). The red background area marks the moment when the rogue wave occurred.

3 RESULT

3.1 Wave parameter threshold analysis

3.1.1 Maximum wave height and wind speed

A comparative analysis of the parameters of the normal and rogue wave clusters is shown in Fig.4, where the blue line in Fig.4a represents the degree of abnormality of the rogue wave. Most of the ratio of the maximum wave height to the effective wave height of the rogue wave group in this sea area ranged 2–3, including 569 small and light waves with $0.1 \leq H_s < 1.25$, 45 medium waves with $1.25 \leq H_s < 2.5$, and only 13 large waves with $2.5 \leq H_s < 4.0$ in the rogue wave train, which indicates that the rogue waves in this sea area tend to occur in the wave group with smaller effective wave heights. The rogue wave clusters in Fig.4b correspond to 90.76% of the wind speeds less than 8 m/s, which are mostly concentrated in $H_s < 1.25$. When the wind speed is greater than 8 m/s, the growth rate of H_s of the rogue wave group is greater than that of the normal wave group, and the dispersion of the rogue wave group is much greater than that of the normal wave group, which suggests that the promotion of the wave height by the high wind speed in this sea area is obviously stronger than that of the low wind speed condition. The moderating role of wind speed in wave development is highlighted.

3.1.2 Wave steepness and spectral width

Wave steepness δ, as a key dimensionless parameter in wave dynamics, quantifies the average geometric slope of the wave profile through the ratio of wave height to wavelength, which not only reflect the nonlinear strength of waves in nonlinear wave regimes, but also serve as a diagnostic index for evaluating the extremity of the marine environment. The wave steepness is defined (Xue et al., 2023) as:

$$\delta = \frac{H_s}{L}. \tag{2}$$

The wavelength is defined as:

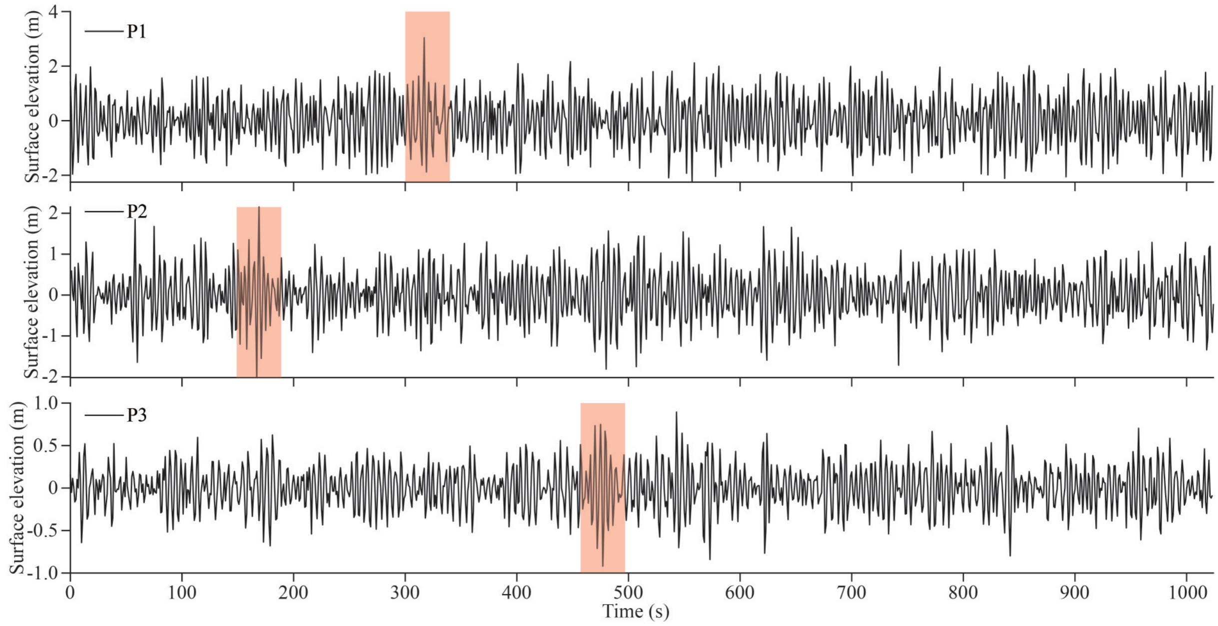

Fig.3 Typical rogue wave sequence

The pink background area marks the moment of rogue wave focusing.

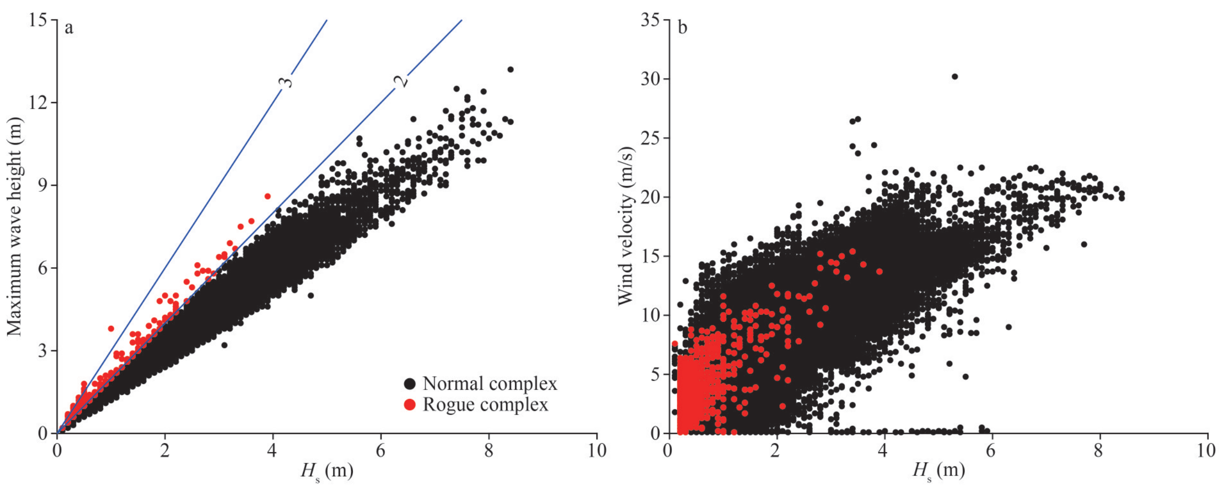

Fig.4 Relationship of effective wave height vs. maximum wave height and wind speed

$$L = \frac{gT_s^2}{2\pi}, \tag{3}$$

where g is the gravitational acceleration and where T_s is the effective wave period.

The spectral width parameter v, a key characteristic quantity of the wave energy spectral distribution, reflects directly the degree of dispersion of the energy distribution of different frequency constituent waves in the wave field, and it is one of the core indices to quantify the intensity of the wave dispersion effect. The spectral width parameter is defined (Fu et al., 2024) as:

$$v = \sqrt{\frac{m_0 m_2}{m_i^2} - 1}, \tag{4}$$

where m_i is the moment of order i of the spectrum, i= 0, 1, 2, and m_i is defined (Hua et al., 2004) as:

$$m_i = \int_0^\infty \omega^i S(\omega)\mathrm{d}\omega, \tag{5}$$

where ω is the wave angular frequency and $S(\omega)$ is the wave spectral density. The modulation instability of waves is caused by nonlinear effects and wave dispersion leading to self-modulation of wave generation in amplitude and frequency. The BFI, as a dimensionless parameter measuring the competing relationship between the nonlinear dynamics of the wave field and the dispersion effects characterizes the threshold for the development of modulation instability; the index determines whether a fluctuating system has entered a state of modulation instability by quantifying the coevolutionary features of the spectral energy distribution and phase correlation. The BFI is defined (Fu et al., 2023) as:

$$\mathrm{BFI}=k_z\sqrt{m_0}\,\nu\sqrt{2\pi}\,, \tag{6}$$

where k_z is the number of waves corresponding to the average period of the wave, which is calculated from the linear dispersion relation.

The rogue wave height ratio H/H_s reflects the maturity of the rogue waves, which can be used to quantify the intensity of nonlinear aggregation of wave energy and reflect the nonequilibrium state statistical characteristics of wave interactions during extreme wave events.

Figure 5 shows the wave steepness and spectral width versus the BFI and H/H_s for the aberrant wave train in this sea area. The wave steepness in Fig.5a is positively correlated with the BFI, and the increased wave nonlinearity whose δ>0.01 promotes modulation instability. In Fig.5b, the spectral width is negatively correlated with the BFI. In particular, the large growth rate with BFI being 0.3–0.05 for ν means that the energy localization effect triggered by the low spectral width exacerbates the nonlinear phase synchronization process by suppressing dispersion expansion, which ultimately triggers the modulation instability of the wave. Numerical analysis revealed that the rogue wave height ratio H/H_s increases with increasing BFI when BFI exceeds the threshold of 0.8. Under this critical condition, the self-focusing effect suppresses the wave-packet broadening effect of dispersion diffusion, at which energy localization is triggered and the anomalous intensity of the rogue wave is increased.

3.1.3 Kurtosis and skewness

The kurtosis of the wave surface elevation distribution, as a fourth-order statistical moment, quantifies the sharp peaks and thick tails characterizing the deviation of the wave field from the Gaussian distribution (kurtosis=3), and represents the third-order nonlinear interactions of waves, wherein the numerical elevation essentially reflects the cumulative effect of the third-order nonlinear dynamic processes on energy redistribution. The kurtosis is defined (Li, 2022) as:

$$\mathrm{kurtosis}=\frac{<(\eta-<\eta>)^4>}{\sigma^4}, \tag{7}$$

where $<\eta>$ denotes the mean value of the wave height over time, σ is the standard deviation of η, and η is the wave surface elevation. The non-zero value of skewness, as a third-order statistical moment, directly characterizes the directionality of energy transport induced by second-order nonlinear interactions in wave field, with positive skewness associated with a long-tailed distribution of steepening peaks and negative skewness corresponding to a statistical distribution of deepening troughs. The skewness was defined (Li, 2022) as:

$$\mathrm{skewness}=\frac{<(\eta-<\eta>)^3>}{\sigma^3}. \tag{8}$$

Based on findings by previous scholars, under the assumptions of unidirectional waves and narrow spectrum, Mori et al. (2011) suggested the following

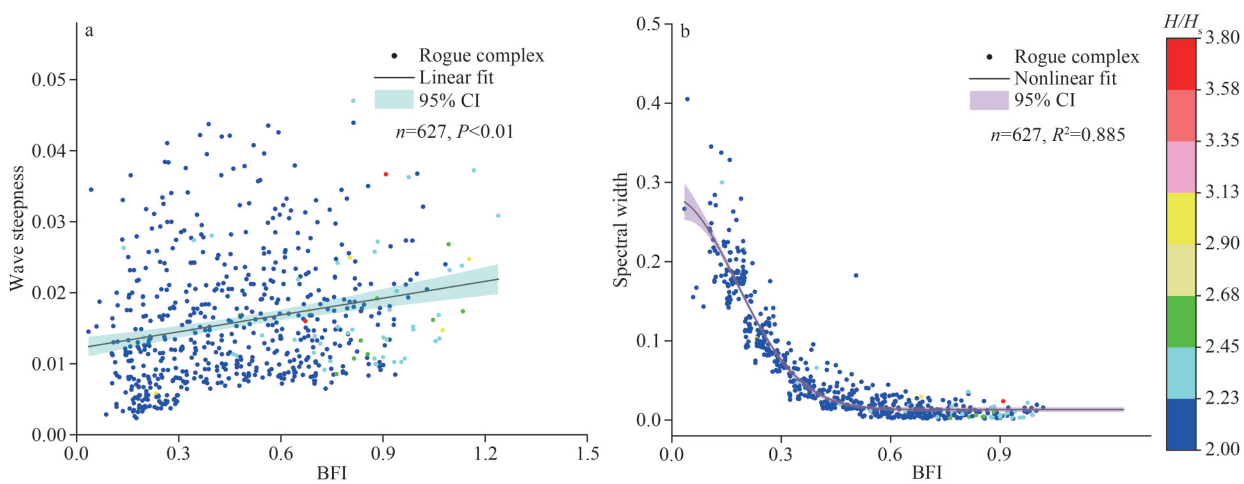

Fig.5 Relationship of BFI index vs. wave steepness (a) and spectral width (b)

relationship between kurtosis and BFI:

$$\text{kurtosis} - 3 = \frac{\pi}{\sqrt{3}} \text{BFI}^2. \quad (9)$$

In this study, we add parameter β to this formula, then:

$$\text{kurtosis} - 3 = \frac{\pi\beta}{\sqrt{3}} \text{BFI}^2. \quad (10)$$

Figure 6 shows the kurtosis versus the BFI and H/H_s for 10 buoys in the sea area. Table 2 shows the parameter β determined from the data of each of the 10 buoys. It can be seen that the values of the parameter β ranges from 0.163 to 0.172, represents the quantitative relationship between kurtosis and BFI in the northern part of the South China Sea. Figure 6 shows that the BFI increases as the degree of kurtosis deviation from the Gaussian distribution increases when kurtosis>3, i.e., the third-order nonlinear interactions of waves have a greater influence on the wave propagation process. Compared with the experimental results of Li et al. (2020), who reported that "the BFI values were basically less than 0.8, only three groups were greater than 0.8, and the deviation of the kurtosis values did not increase with increasing BFI values", the results of Li et al. (2020) were as follows: at BFI values greater than 0.8, the deviation of kurtosis values still increases as the BFI index increases. Figure 7 shows the skewness versus the BFI and H/H_s for 10 buoys in this sea area, the skewness is mainly distributed in the range of -0.1–0.2, and the correlation between the skewness and the BFI is weak, i.e., the second-order nonlinear effect of waves has a weak influence on the wave propagation process, which is consistent with the conclusions of the simulation experiment by Toffoli et al.(2009). In particular, when kurtosis>3 and $2 \leq H/H_s \leq 2.2$, increase in the kurtosis value contributes relatively little to rogue wave. When $H/H_s > 2.2$, the increase in the kurtosis value contributes significantly to the increase in the anomalous intensity of rogue wave.

3.2 Energy analysis

To further investigate the generation mechanism of rogue waves, 60 groups of rogue wave columns were selected from 627 groups for test, and wave data interception was performed for each group of rogue wave columns where they are located. A wavelet transform was taken for 100 s of wave data, including rogue wave data, and three representative sets of rogue wave trains were selected. The wavelet

Table 2 Value of the parameter β

Bouy station	β
S1	0.168
S2	0.172
S3	0.167
S4	0.165
S5	0.168
S6	0.165
S7	0.165
S8	0.163
S9	0.168
S10	0.163

energy spectra of each of these three sets of aberrant wave trains are shown in Fig.8, where the vertical coordinates on the right-hand side of the plot include the wavefront process lines and the energy, which is given in units of $m^2 \cdot s$.

The rogue wave formed by the modulation instability is given in Fig.8a, where an anomalous wave suddenly appears in a longer wave group and the high-frequency energy of the corresponding wavelet energy spectrum is obvious, i.e., the cascade transfer of energy triggered by the nonlinear phase modulation, which reveals the modulation effect of the nonlinear action on the redistribution of wave energy in the process of the rogue wave generation. Figure 8b shows that rogue waves formed by the superposition of the wave packet and those located in a triple wave packet structure conforms to the classic "three-sister wave" pattern. The formation of this anomalous wave starts from the brief aggregation of component waves of different frequencies, which is accompanied mostly by energy redistribution after aggregation, and the energy is transferred through dispersion modulation and eventually decomposed into multiple component waves. The ungrown rogue wave (Fig.8c) shows that the wave height at t=435 s does not reach the rogue wave determination threshold, but its instantaneous wave energy density is greater than of the rogue wave event at t=478 s, i.e., the energy maximum does not occur at the peak maximum of the wave. This mismatch of energy-peak extremes suggests that fully resolving the synergistic mechanisms involved in the generation of such anomalous waves through phase and dispersion modulation, energy transfer, and nonlinear wave interactions is difficult.

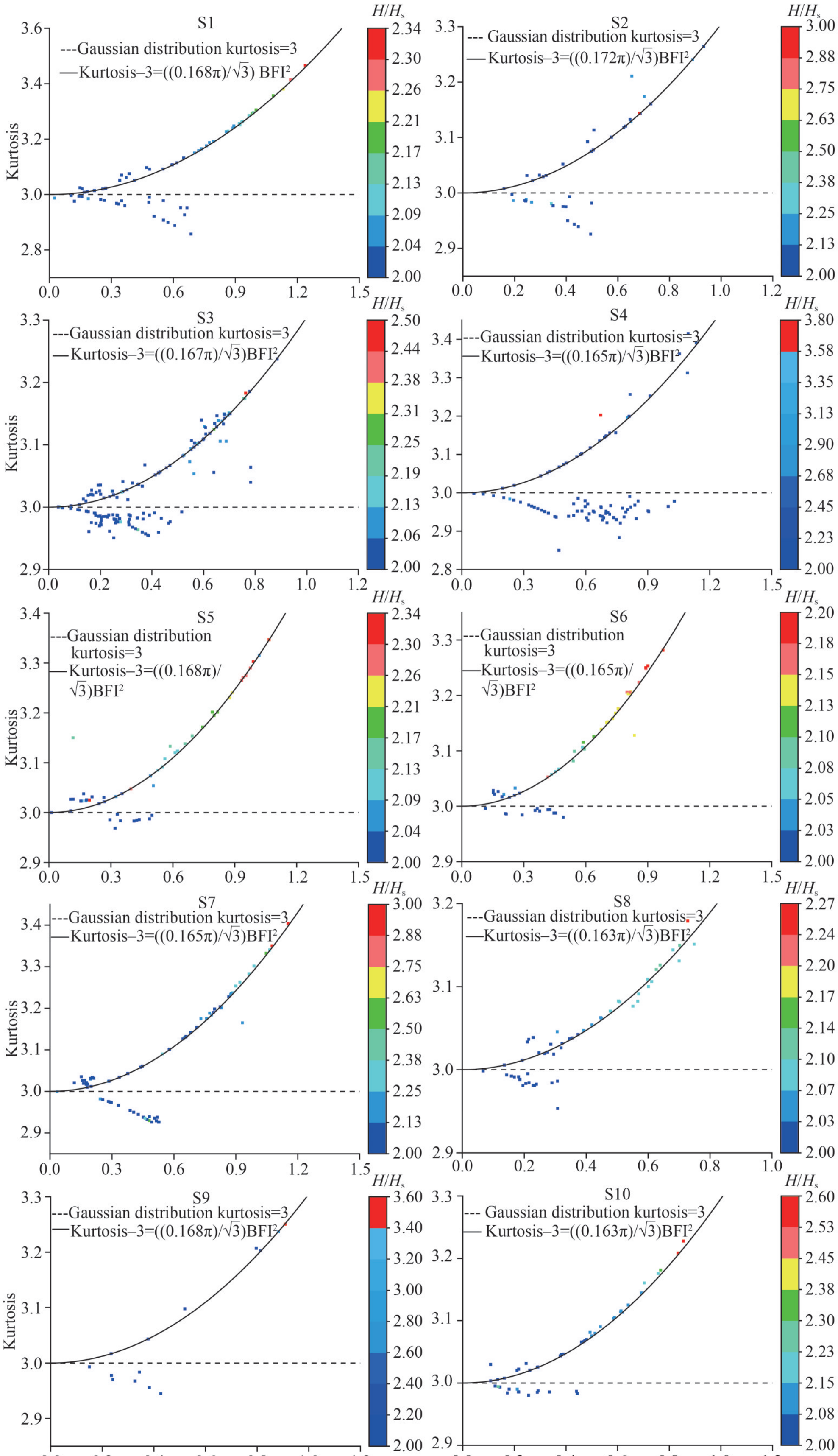

Fig.6 Relationship between kurtosis and BFI index

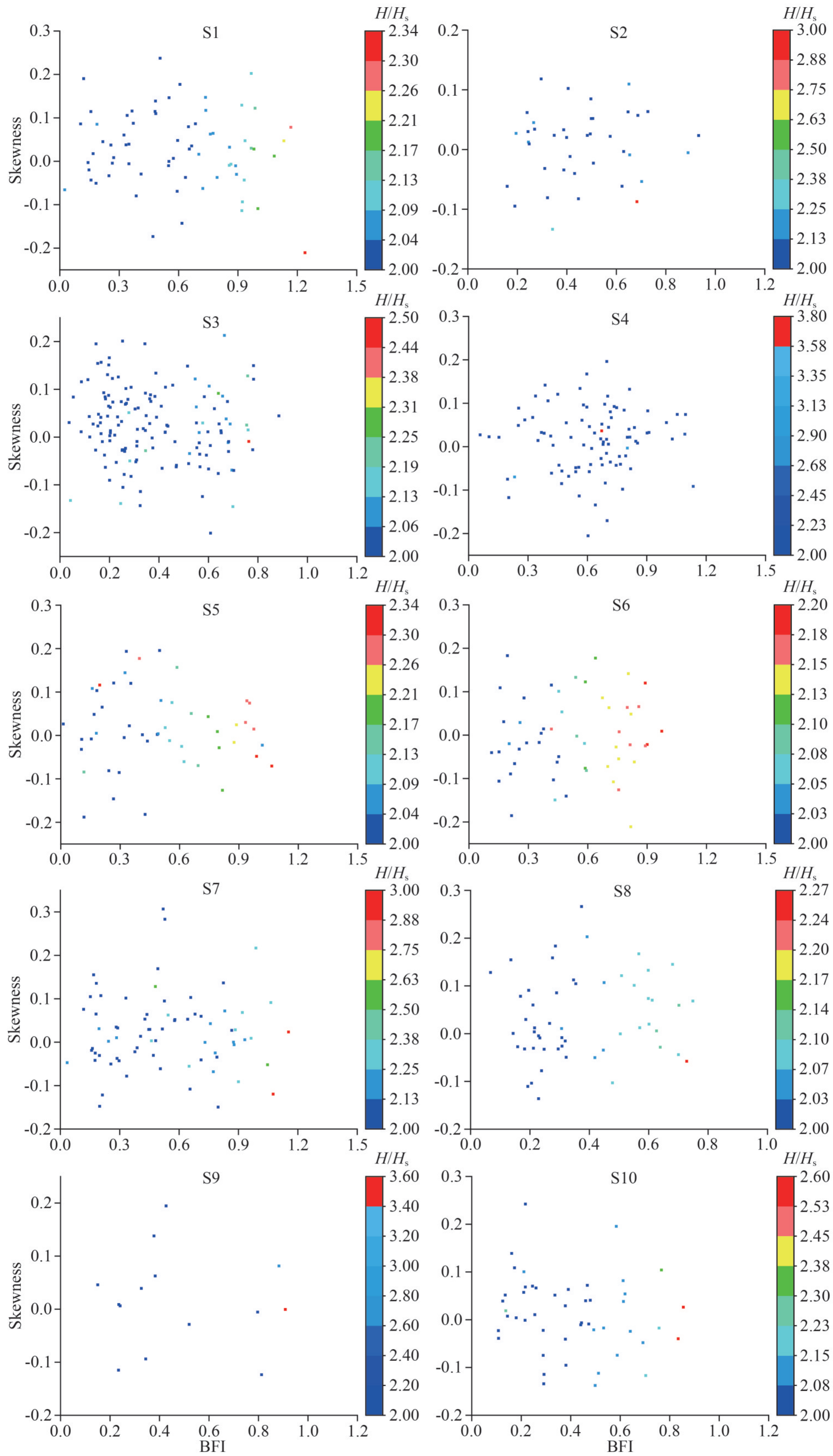

Fig.7 Relationship between skewness and BFI index

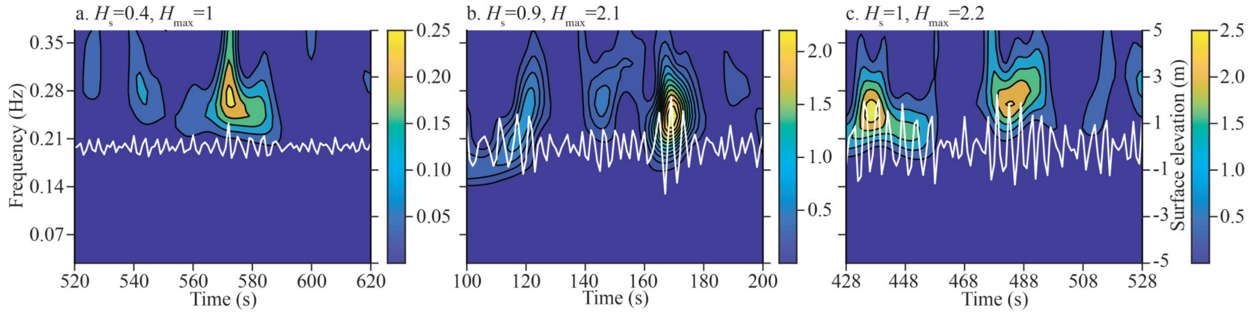

Fig.8 Wavelet energy spectrum

3.3 Chaotic dynamics analysis

Based on previous parameter-scale synergistic statistical dynamic action, dispersion effect and phase modulation, and energy analysis, it remain impossible to resolve completely the generation mechanism of rogue waves. Therefore, the theory of chaotic dynamics is introduced to reduce the continuous dynamic system for discrete mapping via the Poincaré cross-section, and to study the nonlinear dynamic system of the wave train containing rogue waves. The Poincaré cross-section is a graph used to show the evolution in the state of a system over time. By intercepting a sample at a specific point in time, it is possible to observe the quasi-periodicity and determine whether there is a chaotic state in a wave train containing rogue waves.

In this study, 90 out of 627 sets of rogue wave trains were randomly selected for numerical experiments, and the Poincare points (peak state point) were obtained via periodic intercepts at each peak (local maximum) of the wave time series in which each set of rogue waves was located. The wave height derivative corresponding to each wave peak was also determined to indicate the instantaneous velocity of the vertical motion of the wave. Figure 9 shows the Poincare cross-section of the sequence containing three sets of rogue waves.

The rogue waves corresponded to wavefront elevation and wave height derivative that significantly deviate from the normal point region, and the rogue wave points form isolated clusters, which reflected the sudden aggregation of energy. The Poincare cross section shown in Fig.9 exhibited random discrete points, and chaotic motions due to chaotic attractors might be present in the regions with more such points. In contrast, although the Poincaré cross-section can qualitatively analyze the chaotic dynamic properties, it cannot directly quantify the intensity of chaos. The intensity of chaos can be quantitatively analyzed in conjunction with the Lyapunov exponent λ: $0<\lambda\leq0.05$ indicates weak chaos, $0.05<\lambda\leq0.2$ for moderate chaos, and $\lambda>0.2$ for strong chaos. Based on time serial data, using the state points sampled at the wave crest i, we can determine its neighboring point j (j after i to avoid instantaneous neighbors), and track their distances during the time evolution, to calculate their divergence distances with the number of iterations and the number of wave crests, and the mean of the logarithmic growth rates of these distances. Depending on the data length, the maximum time step max (k) is set to 50, and the Lyapunov exponential plots for each wave train are given in Fig.10. The horizontal axis time reflects the evolution in the state of the wave system, and the average divergence rate on the vertical axis is the

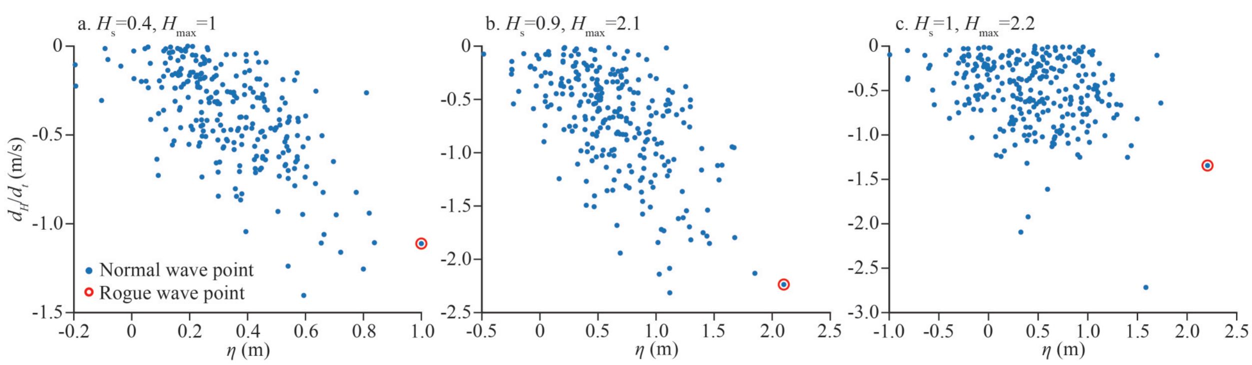

Fig.9 Cross-section of Poincare

separation rate of neighboring trajectories on logarithmic scale, which is directly related to the chaotic properties of the system. The blue solid line is the actual calculated mean dispersion rate trajectory containing information about the dynamic evolution of the system, and the red dashed line is a linear fit based on the first 80% of the data. The slope is the maximum Lyapunov exponent λ. where i, j are the wave state points obtained by simplifying the time series to a discrete mapping in the Poincaré cross section. k is a time step, i.e., a discrete evolutionary step, denoting the number of iterative steps computed from the initial separation point, which represents the evolutionary progress of the trajectory rather than the real time and has no corresponding physical unit (dimensionless).

Figure 10 shows that the curve rises rapidly and steeply when $0<k<5$, and the slope is significantly larger than at later times, i.e., the rapid separation of trajectories at short time scales reflects the sensitive dependence of chaotic systems. When $5\leq k\leq 40$, the curve shows an approximately linear trend, closely followed by the red fitted line, satisfying the exponential dispersion assumption $\ln(d_k)\approx\ln(d_0)+\lambda k$. When $k>40$, the curve has a regional saturation tendency, and the actual values gradually deviate from the fitted line. Because there is a finite amount of energy in real physical systems, trajectory separation does not grow indefinitely. The maximum Lyapunov exponents of the sequences in which the three sets of rogue waves are located are λ_1=0.007 6, λ_2=0.007 1, and λ_3=0.008 7, which are all greater than 0, but less than 0.05, belong to the faint chaos. It is shown that there are chaotic phenomena in this nonlinear system. Moreover, the unresolvable phenomenon in Fig.8c may be a combination of mechanisms including dispersion effects, phase modulation, modulation instability, and chaotic dynamics.

Nonlinear dynamics analysis of a wave train containing a rogue wave shows chaotic features in its system evolution. Quantitative calculations based on the maximum Lyapunov exponent further show that this chaotic property is weaker. This phenomenon may stem from the energy coupling effect between rogue waves in the wave train and the background regular waves, that is, the strong local nonlinear signal of the rogue wave is diluted by the surrounding dominant regular wave, which manifests that the chaotic intensity is weakening on the macroscopic observation scale. This “averaging” effect may be related to the linear superposition of background waves, or it may reflect the intermittent and localized nature of the nonlinear dynamics that characterizes the generation and propagation of the rogue wave. From the basic theory of phase space instability and Lyapunov exponents, we know that $\lambda>0$ indicates that the system is sensitive to initial conditions, and small perturbations will rapidly amplify over time. In phase space, $\lambda>0$ means that the system's orbits will diverge exponentially, and the orbits of adjacent initial states will quickly separate. When the system is in a weak chaotic state, the instability of the phase space prevents energy from being distributed evenly. During the process of disturbance amplification, energy concentrates in specific areas, achieving intermittent energy transport to the focal point and forming a transient energy-focusing phenomenon. Notably, a limitation of this study is the paucity of observational data for wave trains containing multiple rogue waves, which makes it difficult to systematically analyze the evolution law of chaotic properties in the process of multiple rogue wave generation, and limits the in-depth investigation of the correlation between chaotic intensity and rogue wave generation. Nonetheless,

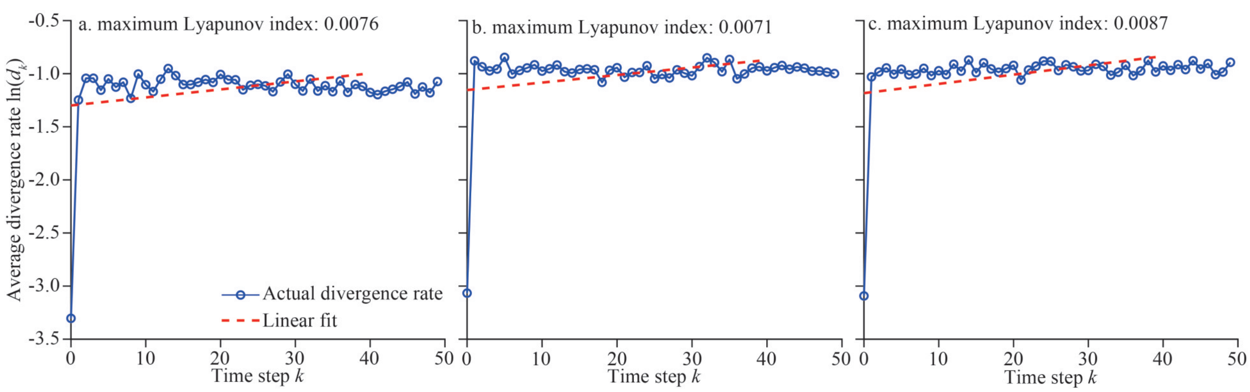

Fig.10 The Lyapunov index

combining nonlinear wave theory with the available results allows for preliminary inferences to be made: when a wave system enters a chaotic state, its intrinsic dynamical stochasticity (e.g., nonstationary transfer of energy over a multiscale range, nonlinear coupling of wave-wave interactions) may provide critical dynamical conditions for the sudden generation of rogue wave, indicating a possible correlation with the generation of rogue wave.

4 DISCUSSION AND CONCLUSION

On the basis of buoy observational data from the northern waters of the South China Sea, wave parameters such as wave steepness, spectral width, kurtosis, skewness and other wave parameters of the wave train where rogue waves located were analyzed in combination with the BFI. The wavelet energy spectrum of the rogue wave process was analyzed by combining the wavelet transforms, and the generation mechanism of rogue wave was also investigated by introducing chaotic dynamics. The following conclusions can be drawn:

(1) Waves in the northern waters of the South China Sea have an elevated BFI under high wave steepness and narrow spectral conditions, which are more likely to trigger wave modulation instability and thus lead to rogue wave events. When the wind speed is high and the effective wave height is small, it is more likely to promote the occurrence of rogue waves.

(2) There is a relationship of Eq.10 between aberrant wave kurtosis and BFI in the northern part of the South China Sea, and the parameter β ranges from 0.163 to 0.172. When kurtosis>3, the BFI increases as the degree of kurtosis deviation from the Gaussian distribution increases, i. e., the third-order nonlinear interaction of waves has a greater influence on the wave propagation process. In particular, when kurtosis>3 and $2\leq H/H_s\leq 2.2$, the increase in kurtosis contributes relatively little to the rogue wave; when $H/H_s>2.2$, the increase in kurtosis contributes significantly to the increase in the anomalous intensity of the rogue wave.

(3) The wavelet energy spectra of the sequences in which the three types of rogue waves are located were analyzed via wavelet transform. Both the rogue waves induced by the modulation instability and the rogue waves induced by the superposition of wave groups can be explained by the energy distribution, energy transfer and redistribution, and phase and dispersion modulation. In contrast, analyzing the generation mechanism of rogue waves that have no sufficient growth from the time domain waveform characteristics and frequency-domain wavelet energy density is difficult.

(4) Rogue waves are studied by introducing chaotic dynamics, qualitatively determining the chaotic behavior from the Poincaré cross-section map and quantitatively analyzing the strength of chaotic systems from the Lyapunov exponential map. According to phase space instability and Lyapunov exponent theory, $\lambda>0$ characterizes the sensitivity of the system to initial conditions, with small perturbations amplifying exponentially over time, causing adjacent orbits in phase space to separate rapidly. In a weak chaotic state, this instability hinders the uniform distribution of energy, causing energy to concentrate in local areas during the disturbance amplification process and forming transient energy focusing. Weak chaotic features can be observed in these wave trains containing rogue waves, which may be due to the strong nonlinear signals of rogue waves being diluted by the surrounding dominant regular waves, resulting in a decrease in chaotic intensity. By combining nonlinear wave theory with existing results, a preliminary inference can be made: when a wave system enters a chaotic state, its intrinsic dynamical stochasticity may provide key dynamic conditions for the sudden generation of rogue waves, which may be related to the generation of rogue waves.

5 DATA AVAILABILITY STATEMENT

All data generated and/or analyzed during this study are available from the corresponding author on reasonable request.

References

Cavaleri L, Barbariol F, Benetazzo A et al. 2016. The Draupner wave: a fresh look and the emerging view. *Journal of Geophysical Research*: *Oceans*, **121**(8): 6061-6075, https://doi.org/10.1002/2016JC011649.

Chen Z Y, Liu D F, Wang F Q. 2019. Study of probability prediction of extreme sea hazards and disaster prevention design criteria at South China Sea. *Periodical of Ocean University of China*, **49**(1): 115-120, https://doi.org/10.16441/j.cnki.hdxb.20160156. (in Chinese with English abstract)

Davis M C. 1966. Testing Ship Models in Transient Waves. PN.

Dyachenko A I, Zakharov V E. 2005. Modulation instability of Stokes wave→freak wave. *Journal of Experimental and Theoretical Physics Letters*, **81**(6): 255-259, https://doi.org/10.1134/1.1931010.

Fu R L, Cai H Y, Tao A F et al. 2023. Researches on characteristics of shapes of freak waves in the Norwegian Sea. *Haiyang Xuebao*, **45**(4): 133-143, https://doi.org/10.12284/hyxb2023031. (in Chinese with English abstract)

Fu R L, Cai H Y, Wang G et al. 2024. Statistics of unidirectional wave groups with and without freak waves observed in the Norwegian Sea. *Physics of Fluids*, **36**(10): 107152, https://doi.org/10.1063/5.0233383.

He Y L, Mao H F, Wu G L et al. 2021. Experimental analysis of the nonlinear geometric characteristics for extreme wave in deep water. *The Ocean Engineering*, **39**(5): 86-94, https://doi.org/10.16483/j.issn.1005-9865.2021.05.009. (in Chinese with English abstract)

Hua F, Fan B, Lu Y et al. 2004. An empirical relation between sea wave spectrum peak period and zero-crossing period. *Advances in Marine Science*, **22**(1): 16-20, https://doi.org/10.3969/j.issn.1671-6647.2004.01.002. (in Chinese with English abstract)

Kriebel D L, Alsina M V. 2000. Simulation of extreme waves in a background random sea. International Offshore and Polar Engineering Conference. ISOPE, 2000, https://doi.org/ISOPE-I-00-219.

Ke S T, Wang S, Zhang W et al. 2021. Comparative analysis of the mechanism of wave propagation and evolution under the coupling effect of wind, waves, and currents. *Journal of Harbin Engineering University*, **42**(9): 1312-1320, https://doi.org/10.11990/jheu.202006036. (in Chinese with English abstract)

Knobler S, Liberzon D, Fedele F. 2022. Large waves and navigation hazards of the Eastern Mediterranean Sea. *Scientific Reports*, **12**(1): 16511, https://doi.org/10.1038/s41598-022-20355-9.

Li A P. 2022. The Investigation of Occurrence Probabilities of Freak Wave in Multi-Directional Irregular Wave Groups. Dalian University of Technology, Dalian, https://doi.org/10.26991/d.cnki.gdllu.2022.002469. (in Chinese with English abstract)

Li J X, Zhang Y R, Liu S X et al. 2020. Analysis of generation mechanism of freak waves based on two wave groups. *Chinese Journal of Hydrodynamics*, **35**(4): 497-504, https://doi.org/10.16076/j.cnki.cjhd.2020.04.011. (in Chinese with English abstract)

Liu S H, Mu L, Liu K X et al. 2013. Research advance and problems in freak waves. *Advances in Earth Sciences*, **28**(6): 665-673, https://doi.org/10.11867/j.issn.1001-8166.2013.06.0665. (in Chinese with English abstract)

Ma X Z, Ma J X, Ma Y X et al. 2020. Research on spatial wave focusing based on non-hydrostatic wave model. *Periodical of Ocean University of China*, **50**(4): 128-135, https://doi.org/10.16441/j.cnki.hdxb.20180059. (in Chinese with English abstract)

Mori N, Onorato M, Janssen P A E M. 2011. On the estimation of the kurtosis in directional sea states for freak wave forecasting. *Journal of Physical Oceanography*, **41**(8): 1484-1497, https://doi.org/10.1175/2011JPO4542.1.

Onorato M, Osborne A R, Serio M et al. 2004. Observation of strongly non-Gaussian statistics for random sea surface gravity waves in wave flume experiments. *Physical Review E*, **70**(6): 067302, https://doi.org/10.1103/PhysRevE.70.067302.

Pei Y G. 2008. The Generation of Freak Waves and its Behaviors. Dalian University of Technology, Dalian. (in Chinese with English abstract)

Pelinovsky E, Kharif C. 2016. Extreme Ocean Waves. 2nd edn. Springer, Cham. p.45-63, https://doi.org/10.1007/978-3-319-21575-4.

Touboul J, Giovanangeli J P, Kharif C et al. 2006. Freak waves under the action of wind: experiments and simulations. *European Journal of Mechanics-B/Fluids*, **25**(5): 662-676, https://doi.org/10.1016/j.euromechflu.2006.02.006.

Toffoli A, Benoit M, Onorato M et al. 2009. The effect of third-order nonlinearity on statistical properties of random directional waves in finite depth. *Nonlinear Processes in Geophysics*, **16**(1): 131-139, https://doi.org/10.5194/npg-16-131-2009.

Xue Q R, Liang S X, Xu Y Y et al. 2023. Research on laboratory generation method of controllable deep water breaking waves. *Haiyang Xuebao*, **45**(4): 46-56, https://doi.org/10.12284/hyxb2023063. (in Chinese with English abstract)

Yang Y, Miao Q S, Wei G H et al. 2017. Quality control methods and application for the oceanic station observed data in the delayed mode. *Ocean Development and Management*, **34**(10): 109-113, https://doi.org/10.20016/j.cnki.hykfygl.2017.10.024. (in Chinese with English abstract)

Yin H Q, Liang S X. 2014. Projections of Typhoon Haiyan wind and waves based on the SWAN model. *China Water Transport*, **14**(6): 105-107, 111, https://doi.org/CNKI:SUN:ZSUX.0.2014-06-046. (in Chinese)

Zakharov V E. 1968. Stability of periodic waves of finite amplitude on the surface of a deep fluid. *Journal of Applied Mechanics and Technical Physics*, **9**(2): 190-194, https://doi.org/10.1007/BF00913182.

Zhang H Y. 2019. Sand Waves near the Shelf Break of Northern South China Sea: Morphology, Mobility and Mechanism. Institute of Oceanology, University of Chinese Academy of Sciences, Qingdao. (in Chinese with English abstract)

Zhang Y Q, Hu J P, Zhang N C. 2009. Efficient simulation of freak waves in random oceanic sea states. *China Ocean Engineering*, **23**(1): 157-165.

Zhao X Z, Sun Z C, Liang S X. 2009. Focusing model for generating 3-D freak waves based on HOS method. *The Ocean Engineering*, **27**(1): 33-39, https://doi.org/10.16483/j.issn.1005-9865.2009.01.011. (in Chinese with English abstract)